




Article

Numerical Study of Low-Specific-Speed Centrifugal Pump Based on Principal Component Analysis

Yangyang Wei ¹, Han Zhu ¹, Quanwang Fan ², Ning Qiu ^{1,*}, Jie Wu ¹ and Weibin Zhang ³¹ National Research Center of Pumps, Jiangsu University, Zhenjiang 212013, China; wyy@ujs.edu.cn (Y.W.)² Zhejiang Fang Wei Testing Technology Co., Ltd., Hangzhou 311122, China³ Key Laboratory of Fluid and Power Machinery (Xihua University), Ministry of Education, Chengdu 610039, China

* Correspondence: qiuning@ujs.edu.cn

Abstract: The characteristics of pressure pulsations in centrifugal pumps have attracted considerable attention. In this study, principal component analysis is used to discuss the pressure pulsations in a centrifugal pump with a low specific speed, and the primary causes for these pressure pulsations are analyzed in conjunction with experimental results. The results indicate that principal component analysis effectively separates the primary modes that influence the flow field characteristics. An excessive wrap angle results in the formation of a backflow vortex on the working face of the blade. Obvious stratification of the zero-order modal pressure indicates that the geometric structure of the impeller is rational and that the transient flow field is stable. The second- and third-order modes are conjugates, and their dominant frequency coincides with the dominant rotating frequency of the impeller, indicating that the pulsations of a single channel are the primary component of the pressure pulsations. The primary frequency (148.54 Hz) of the pressure pulsations at monitoring points distributed across the volute is three times the rotational frequency (49.51 Hz) of the impeller. The different positions and sub-frequencies of the monitoring points mean that the principal component analysis can effectively identify the impeller-induced sub-frequency difference.

Keywords: unsteady flow; centrifugal pump; pressure pulsation; numerical simulation

Citation: Wei, Y.; Zhu, H.; Fan, Q.; Qiu, N.; Wu, J.; Zhang, W. Numerical Study of Low-Specific-Speed Centrifugal Pump Based on Principal Component Analysis. *Water* **2024**, *16*, 1785. <https://doi.org/10.3390/w16131785>

Academic Editor: Giuseppe Pezzinga

Received: 11 May 2024

Revised: 15 June 2024

Accepted: 21 June 2024

Published: 24 June 2024



Copyright: © 2024 by the authors. Licensee MDPI, Basel, Switzerland. This article is an open access article distributed under the terms and conditions of the Creative Commons Attribution (CC BY) license (<https://creativecommons.org/licenses/by/4.0/>).

1. Introduction

Centrifugal pumps are used in numerous fields [1,2]. Complex unsteady flows can cause negative effects such as pressure pulsations, cavitation, vibrations, and noise in centrifugal pumps, resulting in hydraulic loss and threatening the safe and stable operation of pumps [3,4].

Principal component analysis (PCA) is a data-driven algorithm for extracting dynamic information from unsteady experimental measurements or numerical simulations [5]. Guo et al. [6] used PCA to analyze a liquid ring pump and establish a reduced-order model of an unsteady flow field. They discovered that PCA effectively captures the flow characteristics and exhibits a certain epitaxial prediction ability, allowing the flow field distribution to be predicted over a certain sample range. Chen [7] investigated the wake of a flat plate using PCA, capturing the energy difference of the flow field and the main structure of the wake at various aspect ratios. Miyanawala et al. [8] successfully captured the Karman vortex street, shear layer, and near-wall cavitation structure in the wake of a square cylinder through the use of PCA, while Chen [9] applied PCA to an axial compressor and identified the cause of energy dispersion resulting from a high-frequency scheme. Liu et al. [10] analyzed a cavitation flow field using proper orthogonal decomposition and successfully captured the relationship between structural vibrations and cavitation shedding. Wang et al. [11] examined the vortex shedding in the cavitation wake region around a bluff body using PCA and found that the energy of the large-scale vortex structure decreased as the ventilation coefficient increased.

Due to the harmful effects of pressure pulsation of centrifugal pumps, many scholars focus on its mechanisms and control. Chalghoum et al. [12] have used unsteady simulation techniques to study the interaction between the impeller and the tongue of the volute in centrifugal pumps. Berten et al. [13] have experimentally studied the pressure pulsation of high-speed centrifugal pumps under different working conditions. Barzdaiti et al. [14] have measured the pressure pulsation of centrifugal pumps, pointing out that installing a booster pump in the pipeline system can effectively reduce pressure pulsation. Wang et al. [15] have carried out experiments and simulations on the influence of the position of the blade diffuser on the performance of the centrifugal pump. Their results show that the pressure pulsation inside the volute depends on the interaction between the impeller-diffuser and the diffuser-volute. Yang et al. [16] and others have established a compressible simulation method using the Tait equation, pointing out that the weak compressibility of water will affect the amplitude of pressure pulsation at specific frequencies in the pump. Posa et al. [17] have used large eddy simulation methods to study the impact of centrifugal pump matching pressure parts on performance, and they point out that optimizing the geometric structure of the pressure parts can improve the performance of the centrifugal pump. Bükler et al. [18] have pointed out that changes in the speed of a centrifugal pump during operation can cause pressure pulsation, which propagates in the form of sound waves in the pipeline system. Subsequently, they proposed an intelligent control strategy and evaluated its reliability.

Reducing pressure pulsation is one of the key problems to ensure the stability of low-specific-speed centrifugal pumps. This can be achieved by optimizing the structure of hydraulic components. Pei et al. [19] used the particle swarm optimization algorithm to reduce the pressure pulsation caused by the interference between the blade and the spacer tongue on the basis of ensuring the efficiency and head. Based on the traditional multi-objective optimization method, Tong et al. [20] proposed a hybrid optimization solution method based on the gradient optimization theory, which significantly improved the performance of low-specific-speed pumps. Zhang et al. [21] proposed a special staggered impeller to reduce strong pressure pulsations at low specific speeds. Current research on the flow mechanism in low-specific-speed centrifugal pumps is extensive, but the internal relationship between impeller flow and pressure pulsations, particularly regarding the low-frequency characteristics in centrifugal pumps, remains unclear [19–23]. In this paper, the PCA is used to analyze the impeller pressure field and its principal coherent modes for the unsteady flow of a centrifugal pump.

2. Low-Specific-Speed Centrifugal Pump Parameters and Experimental Settings

This work focuses on a centrifugal pump with a low specific speed. As shown in Figure 1, the circumferential direction of the volute contains five pressure monitoring points [24]. The main parameters of the test pump are detailed in Table 1.

Table 1. Primary parameters of the test pump.

Parameters	Value
Number of blades, Z	3
Specific speed, n_s	21
Diameter of inlet pipe, D_s	50 mm
Head, H	80 m
Speed, n	2900 rev/min
Rated flow, Q	10 m ³ /h
Impeller outlet width, b_2	6.5 mm
Outside diameter of impeller, D_2	259 mm
Blade wrap angle, β	190°
Diameter of outlet pipe, D_d	50 mm

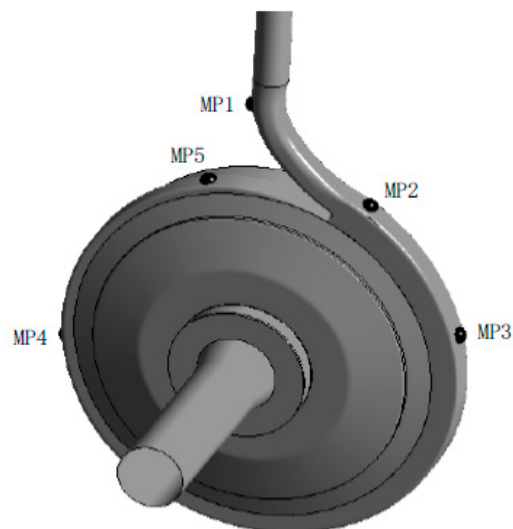


Figure 1. Pressure monitor points.

The relevant experiments were conducted at the National Research Center of Pumps of Jiangsu University, where the test system is as depicted in Figure 2. The experimental system primarily consists of two components: the closed loop and the data acquisition system.

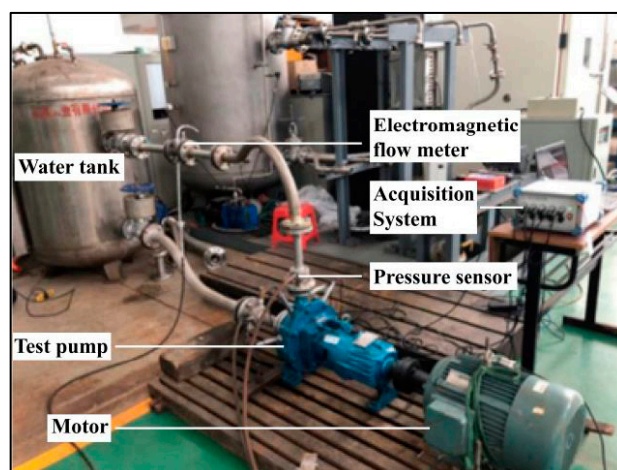


Figure 2. Test system.

3. Numerical Simulation Method

3.1. Basic Governing Equations

In the fluid flow process, matter must be conserved [25,26]. Consequently, the simulations must initially satisfy the continuity equation, which is as follows:

$$\frac{\partial \rho_m}{\partial t} + \frac{\partial(\rho_m u_j)}{\partial x_j} = 0, \quad (1)$$

where j represents the coordinate direction, u represents the velocity, ρ_m represents the mixture density, and x is the displacement along the j direction.

As the flow process involves interphase interactions, the effect of fluid viscosity on the flow must also be taken into account. So, the viscosity of the medium is accounted for in the Navier–Stokes momentum equation, which is expressed in Cartesian coordinates as follows [27,28]:

$$\frac{\partial(\rho_m u_i)}{\partial t} + \frac{\partial(\rho_m u_i u_j)}{\partial x_j} = -\frac{\partial p}{\partial x_i} + \frac{\partial}{\partial x_j} \left[(\mu_m + \mu_t) \left(\frac{\partial u_i}{\partial x_j} + \frac{\partial u_j}{\partial x_i} - \frac{2}{3} \frac{\partial u_i}{\partial x_j} \delta_{ij} \right) \right], \quad (2)$$

where i also represents the coordinate direction and p represents the local pressure, while μ_t and μ_m represent the turbulent and laminar viscosities.

3.2. SST $k-\omega$ Turbulence Model

The original purpose of the SST turbulence model was to capture the near-wall flow structure of airfoils [29]. This model incorporates a hybrid function into the standard model, where the standard $k-\omega$ model is used close to the wall and the standard $k-\epsilon$ model is applied far from the wall [30]. Considering the transfer of turbulent shear stress in turbulent viscosity, the SST $k-\omega$ model is more accurate and dependable than the standard $k-\epsilon$ model.

The SST $k-\omega$ model consists primarily of the turbulent kinetic energy equation, the turbulent frequency equation, and the eddy viscosity equation. Reference [31] describes the turbulent kinetic energy equation as follows:

$$\frac{\partial(\rho k)}{\partial t} + \frac{\partial}{\partial x_j} (\rho U_j k) = \frac{\partial}{\partial x_j} \left[\left(\mu + \frac{\mu_t}{\sigma_k} \right) \frac{\partial k}{\partial x_j} \right] + P_k - \beta^* \rho k \omega. \quad (3)$$

The turbulence eddy frequency equation is stated as follows:

$$\frac{\partial(\rho \omega)}{\partial t} + \frac{\partial}{\partial x_j} (\rho U_j \omega) = \frac{\partial}{\partial x_j} \left[\left(\mu + \frac{\mu_t}{\sigma_\omega} \right) \frac{\partial \omega}{\partial x_j} \right] + \alpha \frac{\omega}{k} P_k - \beta \rho \omega^2 + 2(1 - F_1) \rho \frac{1}{\sigma_{\omega 2} \omega} \frac{\partial k}{\partial x_j} \frac{\partial \omega}{\partial x_j}. \quad (4)$$

The turbulent eddy viscosity equation can be stated as follows:

$$\mu_t = \min \left(\frac{\rho k}{\omega}, \frac{\rho a_1 k}{S F_2} \right), \quad (5)$$

where S is the invariant measure of the strain rate, and the coefficients are defined as follows: $\beta^* = 0.09$, $\alpha = 5/9$, $\sigma_{k1} = 1.1765$, $\sigma_{k2} = 2$, $\sigma_\omega = 2$, $\beta_1 = 0.075$, $\beta_2 = 0.0828$, $\sigma_{\omega 1} = 2$, $\sigma_{\omega 2} = 1/0.856$, and $a_1 = 0.31$.

F_1 and F_2 are two blending functions, the corresponding expressions are as follows:

$$F_1 = \tanh(\Phi_1^4), \quad (6)$$

$$F_2 = \tanh(\Phi_2^2), \quad (7)$$

where

$$\Phi_1 = \min \left(\max \left(\frac{\sqrt{k}}{\beta \omega y}, \frac{500 \mu}{\rho y^2 \omega} \right), \frac{4 \rho k}{\sigma_{\omega 2} D_w^+ y^2} \right), \quad (8)$$

$$D_W^+ = \max \left(2 \rho \frac{1}{\sigma_{\omega 2} \omega} \frac{\partial k}{\partial x_j} \frac{\partial \omega}{\partial x_j}, 1.0 \times 10^{-10} \right), \quad (9)$$

$$\Phi_2 = \max \left(\frac{2 \sqrt{k}}{\beta \omega y}, \frac{500 \mu}{\rho y^2 \omega} \right), \quad (10)$$

where y is the closest distance to the wall, and μ is the laminar dynamic viscosity.

3.3. Simulation Setup and Grid Verification

Both the experimental and simulated water temperatures were maintained at 20 °C. Figure 3 depicts the calculation area and associated conditions. To avoid significant differences between the calculation conditions and experimental working conditions due to

backflow at the inlet and outlet of the calculation domain, an inlet extension is placed in front of the impeller calculation domain, an outlet extension is placed behind the volute calculation domain, and the wall surface is assigned the no-slip condition [32]. The inlet is configured as a 1 atm pressure inlet, while the outlet is configured as a mass flow rate outlet. Other parts are assigned to the static domain, while the impeller is assigned to the rotating domain with a rotational speed of 2900 rpm. The impeller was coupled with the pump chamber, volute, and inlet extension through a dynamic–static junction; it was also coupled to the volute and outlet extension via a static–static junction.

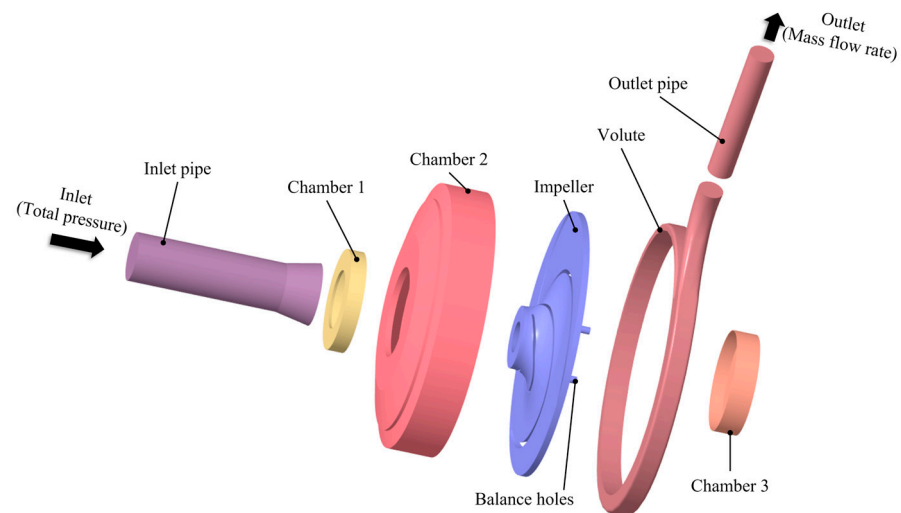


Figure 3. Computational domain structure and boundary conditions.

The transient calculations employ a method of gradual approximation of steady and unsteady flows to generate more accurate simulation results. The total unsteady calculation time is set to 0.2483 s (the time required for the impeller to rotate 12 cycles), with a time step of 5.7471×10^{-4} s (equivalent to 10° rotation of the impeller); each time step is iterated 1–20 times [33] so that the calculation results achieve sufficient convergence accuracy. To ensure the accuracy of the unsteady calculations, the convergence precision is set to 1×10^{-4} .

The ANSYS ICEM 18.0 software was used to divide the hexahedral structured mesh of the calculation model. The SST turbulence model has specific requirements for the near-wall mesh [34]. To guarantee that the outcomes for the simulation calculation are not influenced by variations in mesh quality, a mesh encryption procedure was employed in the near-wall region of the blade to ensure a suitable mesh structure for the boundary layer flow on the blade surface. Figure 4 illustrates the mesh details.

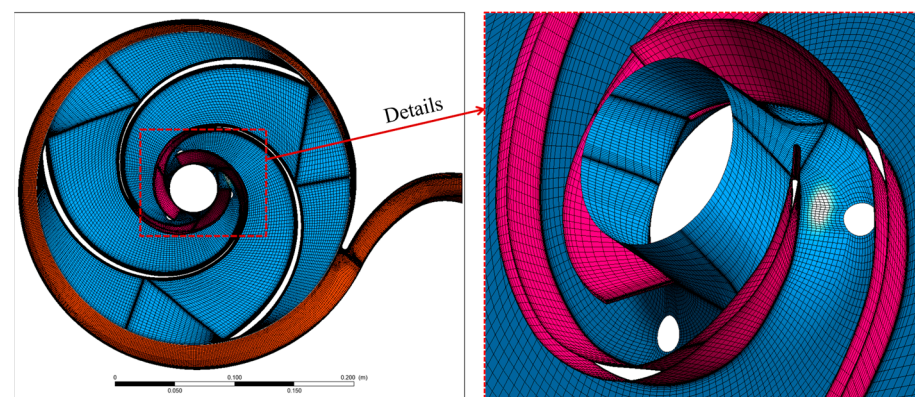


Figure 4. Details of the mesh after division.

The independence of the results from the grid division was evaluated using the change in head. The definition of head is as follows [35]:

$$Head = \frac{P_{out} - P_{in}}{\rho g}, \quad (11)$$

where P_{out} represents the total pressure at the outlet boundary, and P_{in} is the total pressure at the inlet of the calculation domain.

Figure 5 shows the change in head under different grid resolutions. The standard deviation of the head shows that the calculations are reliable. As the grid resolution increases, the head tends to become more stable. Considering the computation time and necessary accuracy, a grid containing 4.1 million cells was chosen for the simulations. As depicted in Figure 6, the y^+ value near the blade wall is less than 30, meeting the calculation requirements of the SST $k-\omega$ turbulence model.

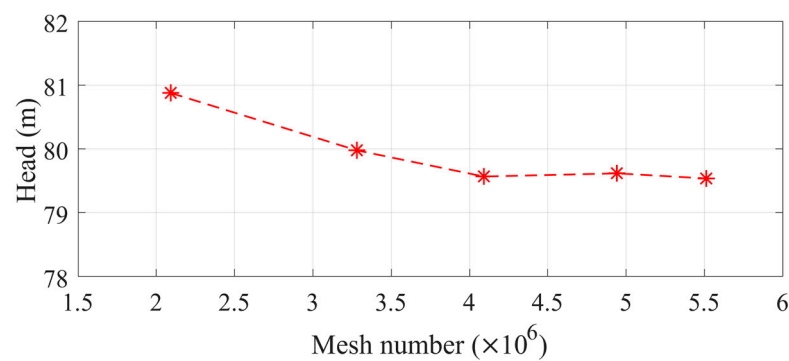


Figure 5. Verification results of grid independence.

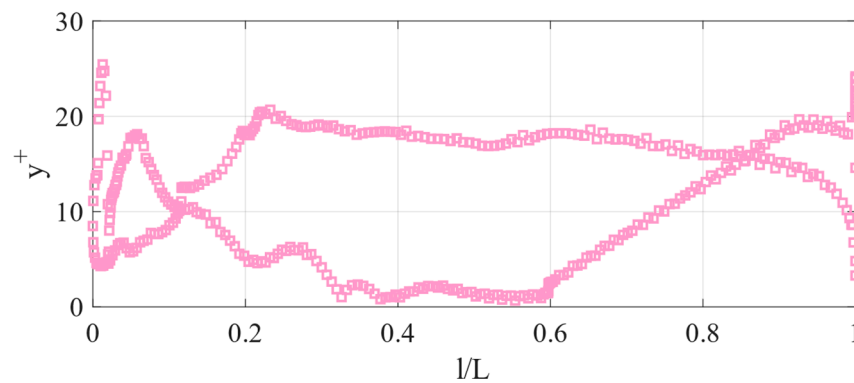


Figure 6. Distribution of y^+ on blades.

4. Principal Component Analysis Method (PCA)

The pressure field in a centrifugal pump can be decomposed into the average flow field and the pulsating flow field [36]. Using N snapshots, the flow field can be described as follows:

$$P(x, t) = \bar{P}(x) + P'(x, t). \quad (12)$$

The average flow field can be expressed as follows:

$$\bar{P}(x) = \frac{1}{N} \sum_{i=1}^N p(x, t_i), \quad (13)$$

where $P'(x, t)$ is the superposition of pulsating flow fields at N times, defined as follows:

$$P'(x, t) = [p'(x, t_1), p'(x, t_2), \dots, p'(x, t_N)]. \quad (14)$$

The fluctuation of the flow field can be expressed by a few modal basis functions and time coefficients as follows:

$$p'(x, t_i) = \sum_{j=1}^N \alpha_j(t_i) \varphi_j, \quad (15)$$

where M is the modal number, and the correlation matrix C can be derived from the pulsating flow field using the following equation:

$$C = P'(x, t)^T P'(x, t), \quad (16)$$

$$C \varphi_j = \lambda_j \varphi_j, \quad (17)$$

where λ_j and φ_j represent the eigenvalues and eigenvectors of the correlation matrix, respectively, and the flow field modes are ordered by their energy based on the size of their eigenvalues. The eigenvectors are orthogonal, and the transient flow field at each time point can be calculated by multiplying the average flow field by the fluctuation of the Q -order modal flow field:

$$p(x, t) = \bar{p}(x) + \sum_{j=1}^{L \text{ mode}} \alpha_j(t_i) \varphi_j, \quad (18)$$

where L is the number of major coherent modes chosen to reconstruct the flow field and the time coefficients are defined as follows:

$$a_j(t_i) = \langle p(x, t_i) \varphi_j \bar{p}(x), \varphi_j \rangle = \langle p'(x, t_i), \varphi_j \rangle. \quad (19)$$

5. Results and Discussion

5.1. Verification of Experimental Results

Figures 7 and 8 compare the simulation and experimental head and efficiency. The trends of the simulated head curve and the experimental results are comparable. When the flow rate is $10.62 \text{ m}^3/\text{h}$, close to the rated operating point, the simulated head is 79.22 m , representing an error of only 0.40% from the experimental result of 79.57 m , which demonstrates the high reliability of the simulations. There are some errors between the simulation and experimental results when operating under biased working conditions, but they are within a reasonable range.

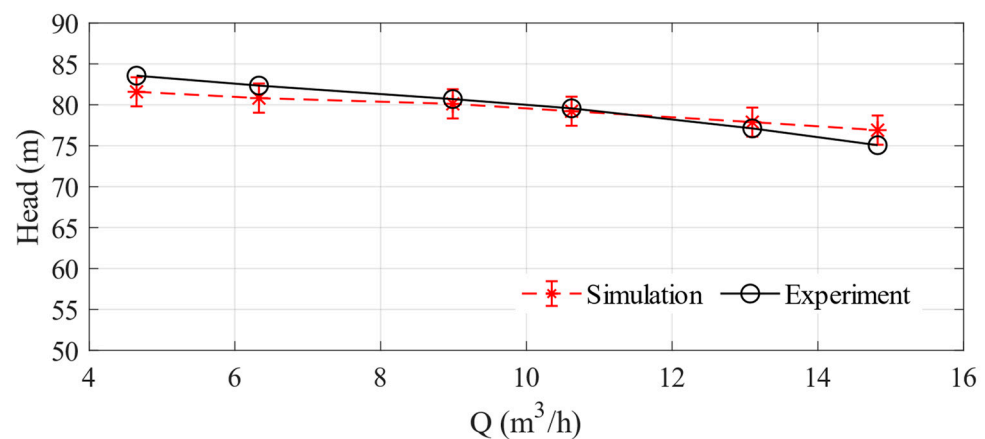


Figure 7. Head comparison.

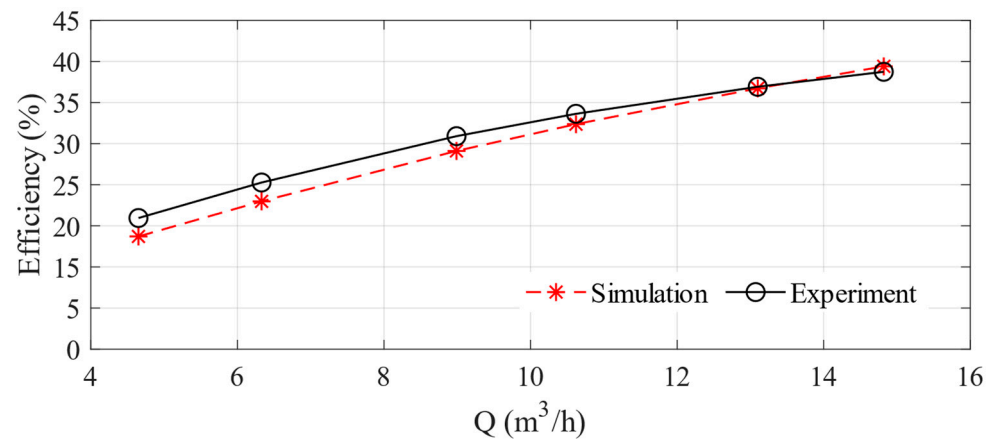


Figure 8. Efficiency comparison.

5.2. Unsteady Flow Analysis

The rotation is counterclockwise from the inlet direction. Figure 9 depicts the section setting for analyzing the flow field using the middle section of the impeller. Figure 10 depicts the velocity streamline distribution at various times under the design conditions, with the flow channel CH1 serving as an analytical reference. Given the large wrap angle, a low-speed backflow vortex (Vortex 1) forms near the blade working face during impeller rotation, resulting in the loss of blade work and a reduction in centrifugal pump performance. In addition, the existence of the balance hole causes fluid leakage in the impeller, which results in a high average velocity at the location of the balance hole. As the blade performs rotary work, the time-averaged fluid velocity in a single channel is clearly stratified, with the working face velocity being lower than the back velocity. The thickness line increases from the inlet to the outlet of the blade, resulting in a low-speed wake at the outlet of the blade (as depicted in Area 1 of the figure) and a loss of performance. The blade performance can be enhanced by reducing the outlet thickness of the working face. The presence of the diaphragm causes a portion of the kinetic energy of the fluid to be converted into pressure energy. During the gradual expansion of the spiral section of the volute, this portion of the pressure energy will be converted into kinetic energy. This can be expressed as a local speed increase during the continued work of the blade on the fluid, as depicted in Region 2 of Figure 10.

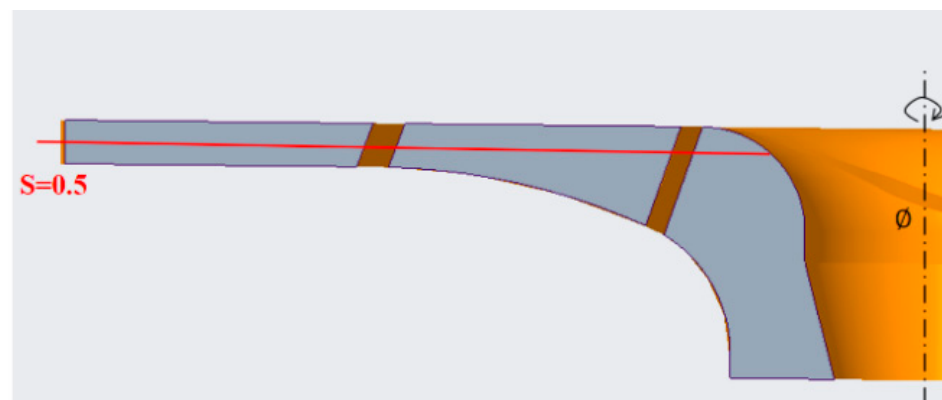


Figure 9. Analyzing cross-section settings.

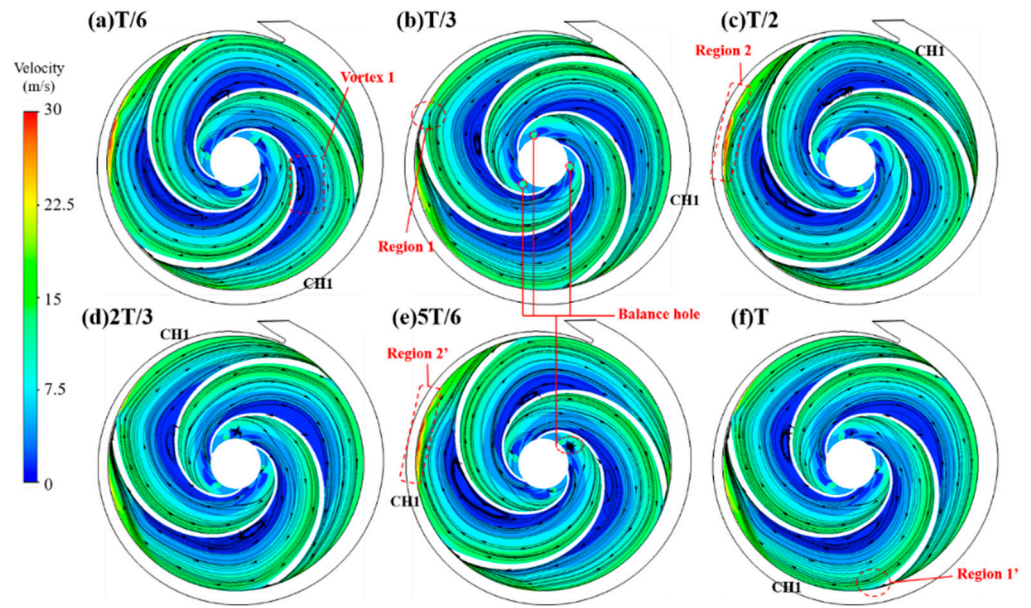


Figure 10. Velocity streamline distribution at different times.

Figure 11 depicts pressure contours at various times. The fluid entering the impeller axially collides with the impeller back cover, resulting in the formation of an irregular low-pressure region at the inlet. During the flow process from the inlet to the outlet of the flow channel, when the blades are in operation, the pressure gradually rises, and the contour of the pressure gradient is clear. As shown in Figure 10, under the interference of the volute, the maximum pressure corresponding to the smaller cross-section of the volute is greater than the maximum pressure of the flow channel closer to the outlet (b). Under the large wrap angle, fluid with high energy is primarily generated near the blade outlets. As depicted in Region 1 of Figure 11, the presence of the diaphragm converts a portion of the fluid kinetic energy into pressure energy, and the high-energy fluid mass is subjected to further work by the blades, resulting in localized areas of high pressure. The low-velocity wake produced by the thicker blade outlet is a high-pressure region, reflecting the partial loss of blade function.

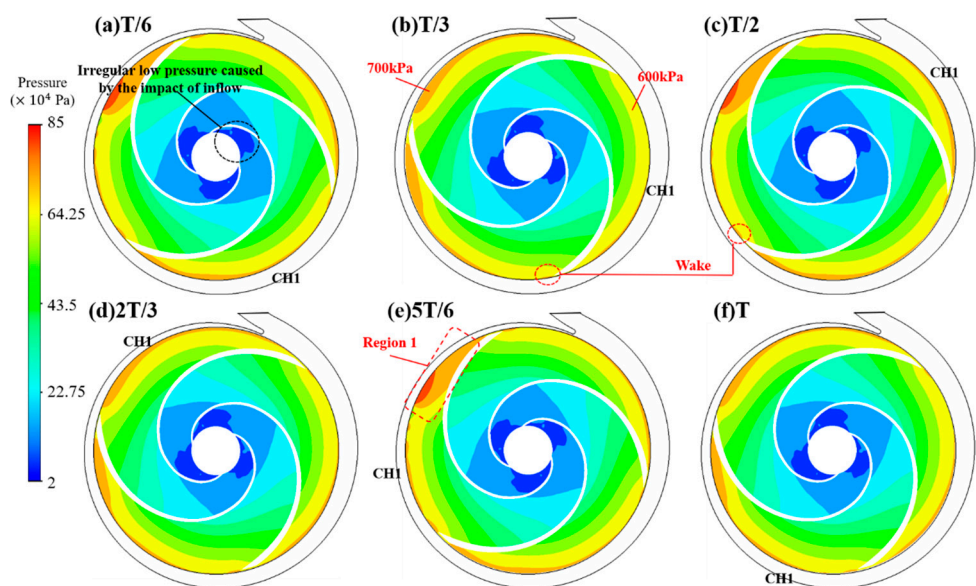


Figure 11. Pressure contours at different times.

5.3. Modal Analysis

PCA is used to reduce the order of the impeller field and analyze the various factors influencing impeller performance in unsteady flow. The reduced energy series of the impeller field is depicted in Figure 12.

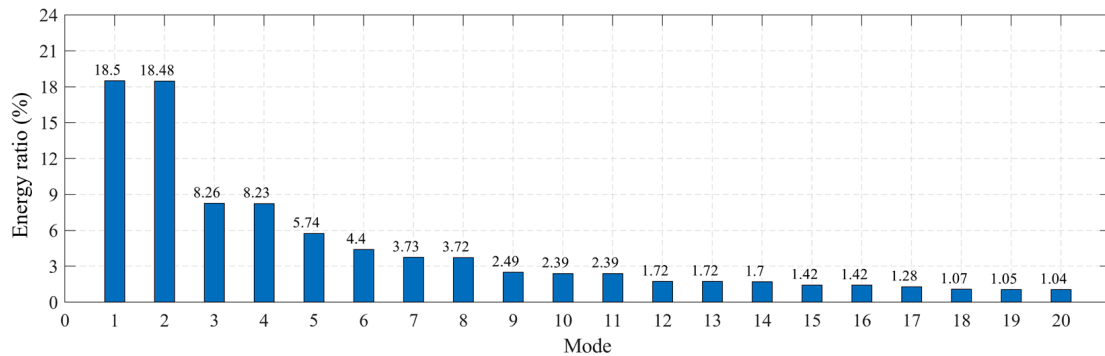


Figure 12. Energy ratio about the absolute pressure of the impeller domain.

The first-order modal energy of pressure comprises 18.50% of the total energy, while the second-order energy comprises 18.48%. As the mode order increases, the energy ratio gradually decreases. Compared with non-rotating flow fields (such as the flow around a cylinder and hydrofoil cavitation), the first-order mode has a lower energy ratio. The modes required for flow field reconstruction should account for more than 95% of the total energy, so the impeller requires a greater number of modal orders for modal restoration.

To analyze the causes of the impeller pressure pulsations, the coefficient time-frequency characteristics and basic functions of the corresponding modes are analyzed. Figure 13 depicts the modal basis function of the impeller pressure field, with panels (a)–(f) representing the various modes. Among them, the zero-order mode represents the time-averaged result of the flow field, and the time-averaged pressure stratification in a single flow channel is evident during the blade rotation. The presence of a balance hole causes fluid to leak from the impeller, resulting in the lowest pressure region.

Positive and negative values of the modal basis function represent local flow changes. The modal basis function represents the variation gradient of physical quantities. The first-order mode shown in Figure 13b and the second-order mode shown in Figure 13c are conjugate modes. After a 120° counterclockwise rotation of the second-order mode, the pulsation positions of the modal basis functions coincide, but the positive and negative values are inverted. The pulsations of the first-order modal basis function are dominated by positive values that fill the entire CH1 channel, with some pulsations also present in the CH2 and CH3 channels. The third- and fourth-order modes are also conjugates, and the fourth-order mode coincides with the pulsation position of the third-order mode after rotating 120° counterclockwise. Similar to the structure of high-energy pulsating clusters distributed throughout different flow passages, the fifth-order mode is a dynamic structure related to the number of blades.

Figure 14 depicts the time-frequency characteristics of the modal coefficients after the order of the impeller velocity field has been decreased. The waveforms of the first- and second-order modes are identical, but have a phase difference and obvious conjugate characteristics, whereas the waveforms of the third- and fourth-order modes exhibit the same pulsating pattern. As shown in Figure 14, for the first, third, and fifth modes, the amplitude of the modal coefficient gradually decreases as the mode number increases.

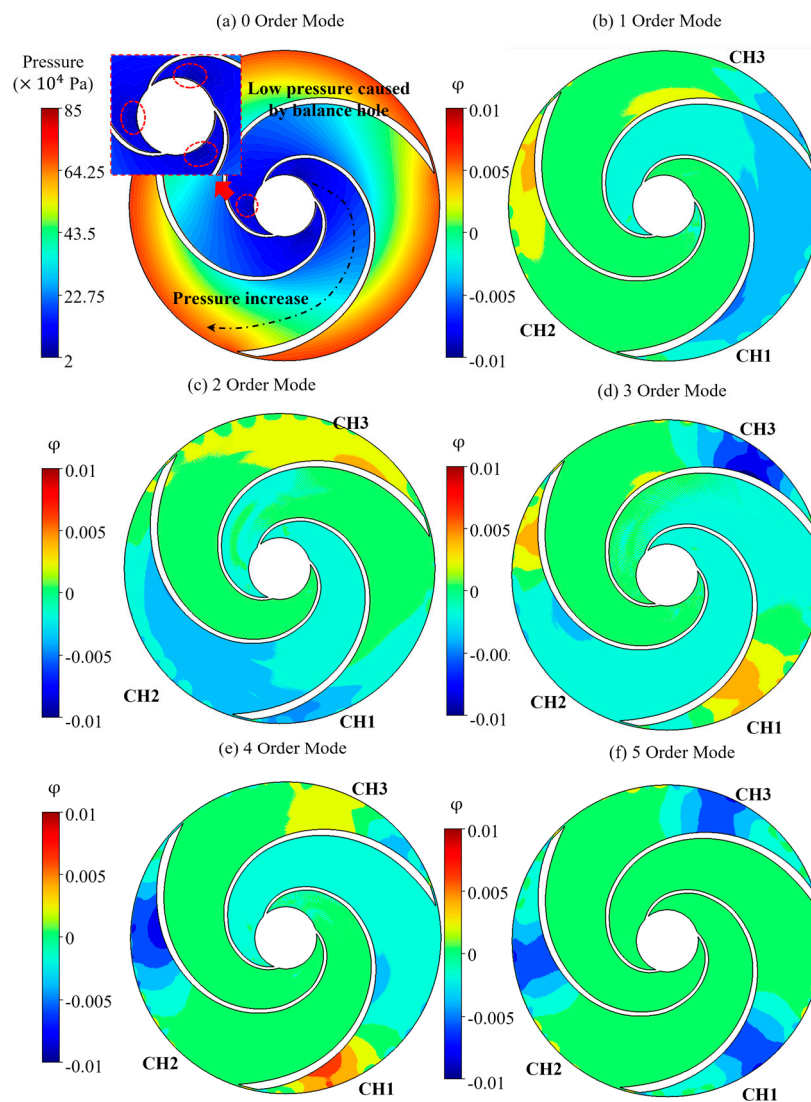


Figure 13. Modal basis function of the impeller pressure field.

The main frequency of the first- and second-order mode coefficients is 48.33 Hz, which is consistent with the frequency of impeller rotation. This indicates that these two modes primarily reflect the pressure pulsations in a single flow channel, corresponding to the pulsations in Figure 13b,c. As there is no coherent positive and negative pulsation change, the corresponding pulsations are independent of the dynamic and static interference caused by the coupling of the volute and impeller. The dominant frequency of the third- and fourth-order modal coefficients is 96.67 Hz. As shown in Figure 13d two of the three channels are dominated by pulsating positive and negative coherent structures (channels CH1 and CH2), so they exhibit the second frequency of rotational speed. The presence of both positive and negative coherent structures in a single channel is a result of flow interference by the volute. The dominant frequency of the fifth-order mode is 145 Hz, which corresponds to the pressure fluctuation characteristics shared by all three channels in Figure 13f.

5.4. Relationship between Modal Characteristics and Pressure Fluctuations

PCA decomposition indicates that the modal characteristics of various orders have a correlation with the pressure pulsations. The pressure fluctuations at five monitoring points are depicted in Figure 15. The pressure fluctuations at the outlet of the volute (MP1) have the highest root mean square value. As the cross-sectional area of the spiral section of the volute decreases, so does the root mean square value, the pressure level, and the fluctuation

amplitude. The frequency-domain characteristics of various pressure monitoring points are depicted in Figure 15b. The relative error between the experimental rotation frequency ($148.54/3 = 49.51$ Hz) and the theoretical rotation frequency ($1/60 \times 2900 = 48.33$ Hz) is 2.36%. Thus, the results can be considered reliable.

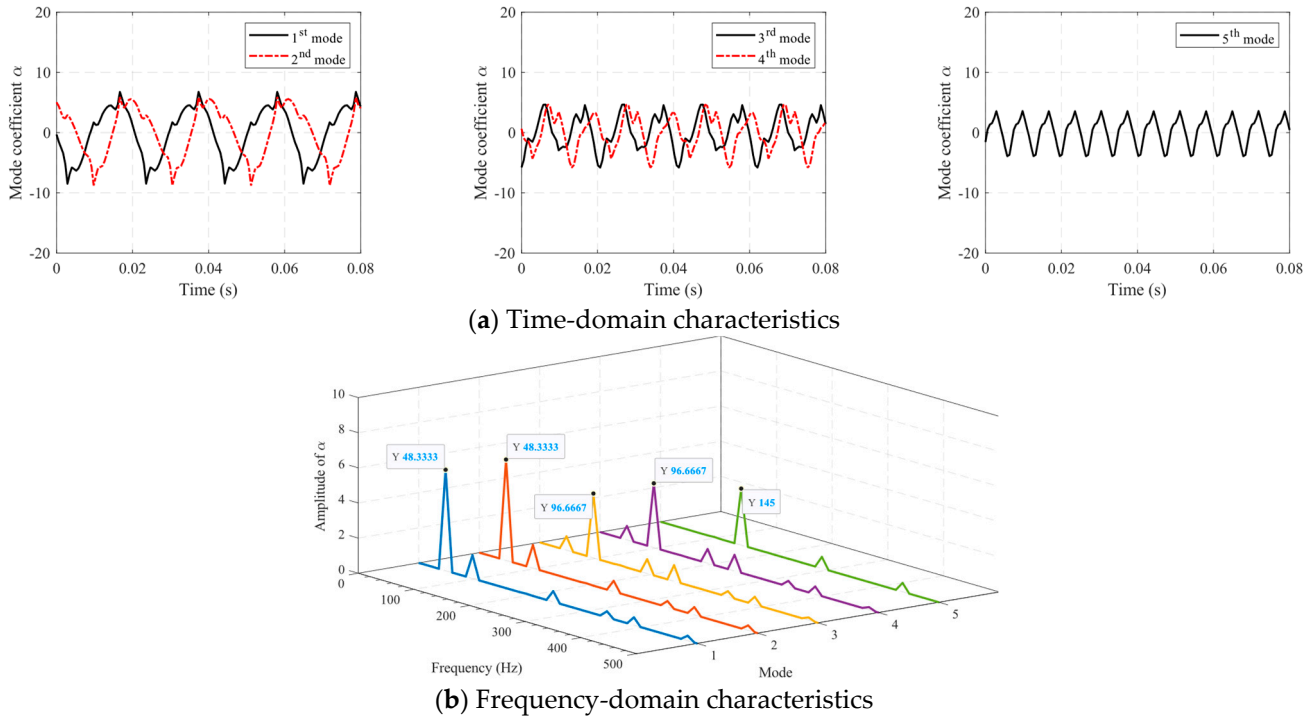


Figure 14. Time-frequency characteristics of the modal coefficient α .

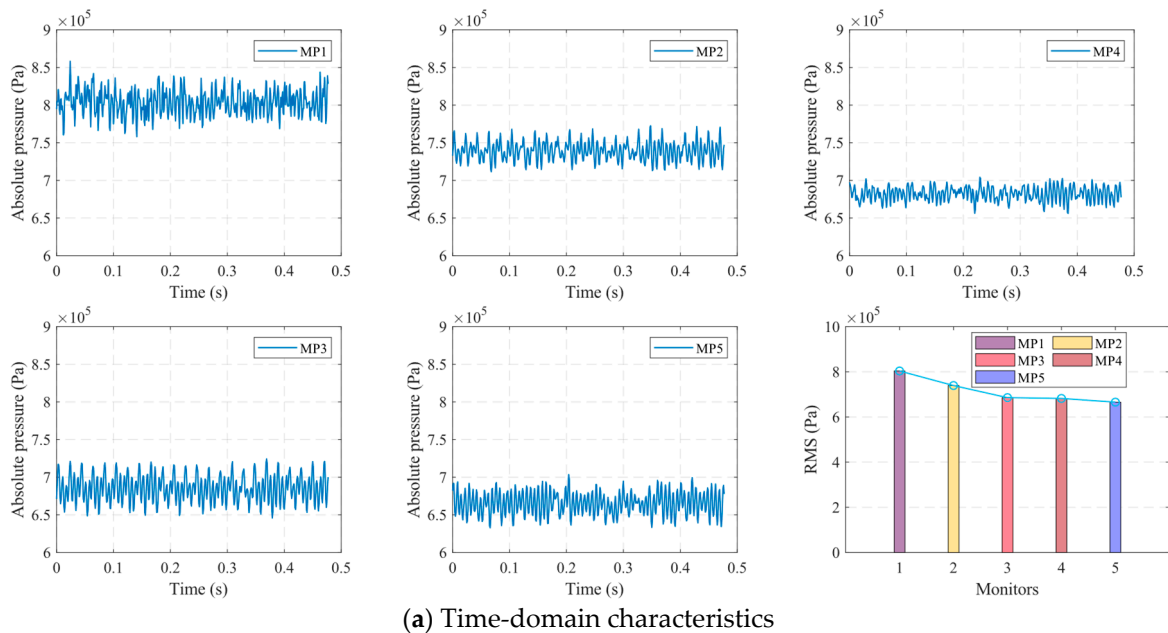
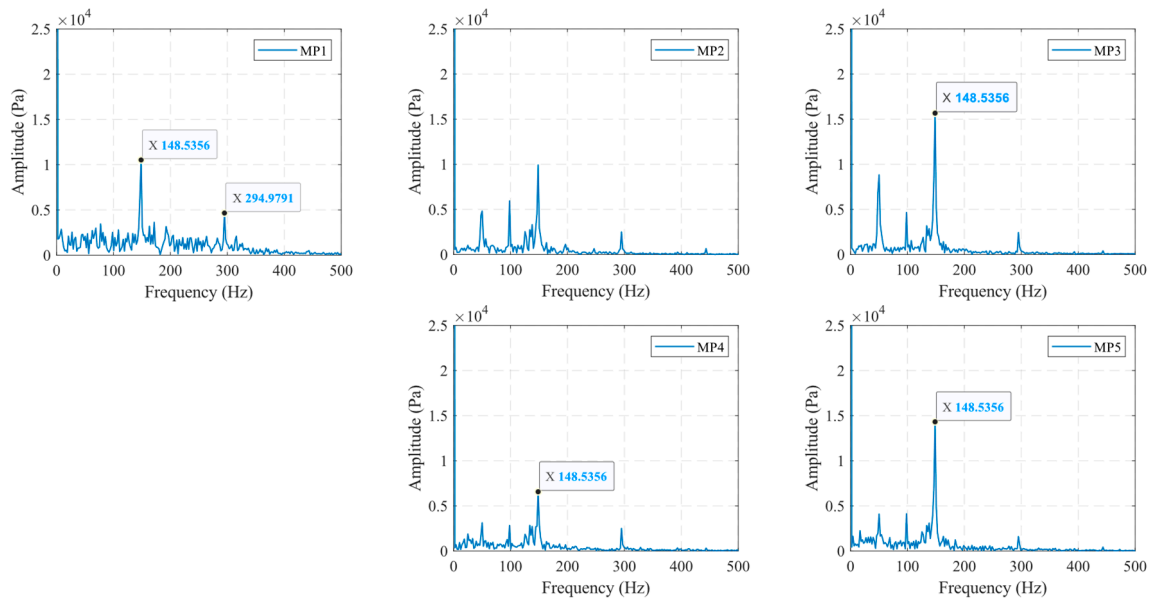


Figure 15. Cont.



(b) Frequency-domain characteristics

Figure 15. Time-frequency characteristics of the pressure pulsation.

It can be seen by combining Figures 15 and 16, at the outlet of the volute, high-energy fluid is created by three blades, and the main frequency is three times the rotation frequency (148.54 Hz). When the subsequent mass fluid flows through this location, the pressure pulsations caused by the previous mass fluid have not dissipated, resulting in a secondary frequency of six times the rotation frequency (299.98 Hz). Monitoring point MP2 is located near the diaphragm tongue on the outlet wall of the volute. Using time T as an example, the pressure pulsation field restored by different modes reveals that the pulsation intensity of the third and fourth modes in this region is greater than that of the first and second modes. Hence, the secondary frequency of pulsations in this region is 99.02 Hz. As the volute section becomes smaller, the amplitude of the first and second modes becomes greater than that of the third and fourth modes. For example, at monitoring point MP3, this results in a sub-frequency of 49.51 Hz. The proximity of MP4 and MP5 to the diaphragm and the small cross-section of the volute means that sub-frequency pulsations are not readily apparent, and the primary frequency is three times the rotation frequency, i.e., 148.54 Hz.

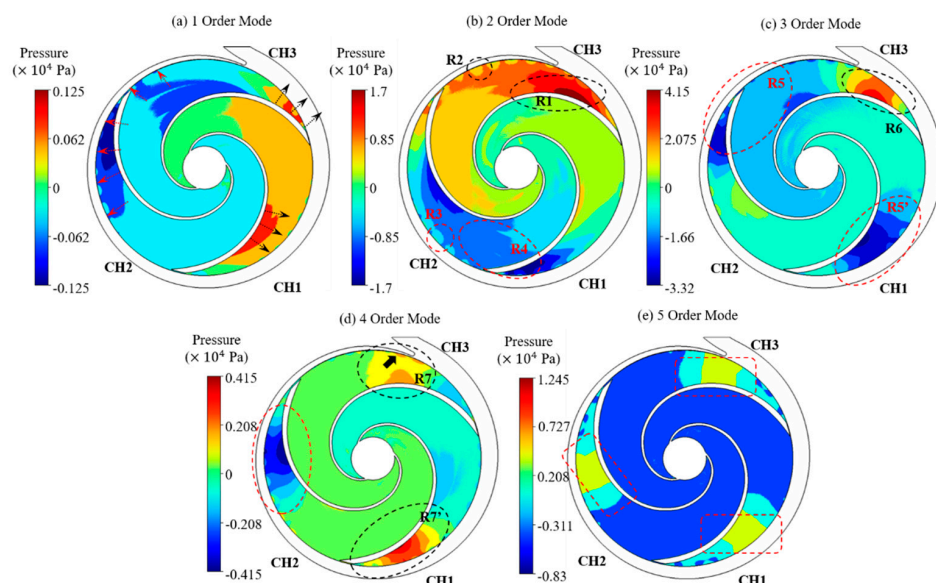


Figure 16. Pressure pulsation after reduction of different modes (T = 0 s).

6. Conclusions

In this study, principal component analysis is used to discuss the pressure pulsations in a centrifugal pump with a low specific speed, and the primary causes for these pressure pulsations are analyzed in conjunction with experimental results. The conclusions may be summarized as follows:

- (1) The internal flow of a low-specific-speed centrifugal pump is complex. If the wrap angle is too long, a backflow vortex will form on the blade's working surface, and a thicker blade outlet will result in the emergence of a wake vortex, which will impair the impeller's performance.
- (2) Using the PCA reduced-order method, the primary modes of the reaction flow field were extracted. The zero-order mode is the time-averaged flow field distribution, and the regular pressure contour reflects both the reasonable geometric structure of the impeller and the stable transient flow field. Mode orders 2–5 represent the distribution and frequency of pressure pulsations caused by the impeller rotation and the dynamic and static interference. The second and third orders are conjugate modes, and their principal frequencies coincide with the principal frequencies of impeller rotation, indicating that the pulsations of a single channel are the primary component of the pressure pulsations.
- (3) The principal frequency of pressure pulsations within the volute is three times the rotational frequency of the impeller. However, the secondary frequencies are different at each monitoring point. The PCA reduced-order method can effectively identify the impeller-induced secondary frequency difference.

Author Contributions: Data curation, J.W.; Funding acquisition, N.Q. and W.Z.; Investigation, H.Z. and Q.F.; Methodology, H.Z. and N.Q.; Software, H.Z. and N.Q.; Validation, N.Q.; Visualization, H.Z.; Writing—original draft, H.Z.; Writing—review and editing, Y.W. and N.Q. All authors have read and agreed to the published version of the manuscript.

Funding: This study is supported by the Science and Technology Support Program of Taizhou City (No. TG202320), the Open Research Subject of Key Laboratory of Fluid and Power Machinery (Xihua University), the Ministry of Education (No. LTDL-2023009), and the National Natural Science Foundation of China (No. 51806082).

Data Availability Statement: The original contributions presented in the study are included in the article, further inquiries can be directed to the corresponding author.

Acknowledgments: We would like to thank the anonymous reviewers for their critical suggestions that have greatly improved this manuscript.

Conflicts of Interest: Author Quanwang Fan was employed by the company Zhejiang Fang Wei Testing Technology Co., Ltd. The remaining authors declare that the research was conducted in the absence of any commercial or financial relationships that could be construed as a potential conflict of interest.

References

1. Jaatinen-Värri, A.; Honkatukia, J.; Uusitalo, A.; Turunen-Saaresti, T. Centrifugal compressor design for high-temperature heat pumps. *Appl. Therm. Eng.* **2024**, *239*, 122087. [[CrossRef](#)]
2. Posa, A. LES study on the influence of the diffuser inlet angle of a centrifugal pump on pressure fluctuations. *Int. J. Heat Fluid Flow* **2021**, *89*, 108804. [[CrossRef](#)]
3. Gülich, J.F. *Centrifugal Pumps*; Springer: Berlin/Heidelberg, Germany, 2008.
4. Karakas, E.S.; Tokgöz, N.; Watanabe, H.; Aureli, M.; Evrensel, C.A. Comparison of Transport Equation-Based Cavitation Models and Application To Industrial Pumps With Inducers. *J. Fluids Eng.* **2022**, *144*, 011201. [[CrossRef](#)]
5. Higham, J.E.; Brevis, W.; Keylock, C.J. Implications of the selection of a particular modal decomposition technique for the analysis of shallow flows. *J. Hydraul. Res.* **2018**, *56*, 796–805. [[CrossRef](#)]
6. Guo, G.; Zhang, R.; Chen, X.; Jiang, L. Analysis of transient gas-liquid two-phase flow in liquid-ring pump based on POD method decomposition. *J. Eng. Thermophys.* **2021**, *42*, 349–356.
7. Chen, L. Research on Wake Structure and Force Characteristics of a Flat Plate with Attached Splitters. Master's Thesis, Zhejiang University, Hangzhou, China, 2020.

8. Miyanawala, T.P.; Jaiman, R.K. Decomposition of wake dynamics in fluid–structure interaction via low-dimensional models. *J. Fluid Mech.* **2019**, *867*, 723–764. [[CrossRef](#)]
9. Chen, C. Investigation of Flow Separation Control and Optimization of Vortex Generator Jets for Axial Flow Compressor. Ph.D. Thesis, Harbin Institute of Technology University, Harbin, China, 2020.
10. Liu, Y.; Long, J.; Wu, Q.; Huang, B.; Wang, G. Data-driven modal decomposition of transient cavitating flow. *Phys. Fluids* **2021**, *33*, 113316. [[CrossRef](#)]
11. Wang, Z.; Zhang, M.; Kong, D.; Huang, B.; Wang, G.; Wang, C. The influence of ventilated cavitation on vortex shedding behind a bluff body. *Exp. Therm. Fluid Sci.* **2018**, *98*, 181–194. [[CrossRef](#)]
12. Chalghoum, I.; Elaoud, S.; Kanfoudi, H.; Akrouit, M. The effects of the rotor-stator interaction on unsteady pressure pulsation and radial force in a centrifugal pump. *J. Hydrodyn.* **2018**, *30*, 672–681. [[CrossRef](#)]
13. Berten, S.; Farhat, M.; Avellan, F.; Dupont, P. Experimental investigation of pressure fluctuations in a high-energy centrifugal pump stage at off-design conditions. In Proceedings of the 12th European Fluid Machinery Congress, Edinburgh, UK, 6–7 October 2014; p. 10.
14. Barzdaitis, V.; Mažeika, P.; Vasylius, M.; Kartašovas, V.; Tadžijevs, A. Investigation of pressure pulsations in centrifugal pump system. *J. Vibroeng.* **2016**, *18*, 1849–1860. [[CrossRef](#)]
15. Wang, W.; Pei, J.; Yuan, S.; Yin, T. Experimental investigation on clocking effect of vaned diffuser on performance characteristics and pressure pulsations in a centrifugal pump. *Exp. Therm. Fluid Sci.* **2018**, *90*, 286–298. [[CrossRef](#)]
16. Yang, J.; Liu, J.; Liu, X.; Xie, T. Numerical Study of Pressure Pulsation of Centrifugal Pumps with the Compressible Mode. *J. Therm. Sci.* **2018**, *28*, 106–114. [[CrossRef](#)]
17. Posa, A.; Lippolis, A. Effect of working conditions and diffuser setting angle on pressure fluctuations within a centrifugal pump. *Int. J. Heat Fluid Flow* **2019**, *75*, 44–60. [[CrossRef](#)]
18. Büker, J.; Laß, A.; Romig, S.; Werner, P.; Wurm, F.-H. On the effect of an ANC system towards the transient pressure fluctuations caused by smart-grid controlled centrifugal pumps. *Appl. Acoust.* **2023**, *209*, 109372. [[CrossRef](#)]
19. Pei, J.; Wang, W.; Yuan, S.; Zhang, J. Optimization on the impeller of a low-specific-speed centrifugal pump for hydraulic performance improvement. *Chin. J. Mech. Eng.* **2016**, *29*, 992–1002. [[CrossRef](#)]
20. Tong, Z.; Xin, J.; Ling, C. Many-Objective Hybrid Optimization Method for Impeller Profile Design of Low Specific Speed Centrifugal Pump in District Energy Systems. *Sustainability* **2021**, *13*, 10537. [[CrossRef](#)]
21. Jiang, J.; Zhang, N.; Liu, X.; Gao, B.; Cao, P. Effect of the staggered impeller on reducing unsteady pressure pulsations of a centrifugal pump. *Energy Sci. Eng.* **2021**, *10*, 194–207. [[CrossRef](#)]
22. Shojaeefard, M.H.; Sareman, S. Analyzing the impact of blade geometrical parameters on energy recovery and efficiency of centrifugal pump as turbine installed in the pressure-reducing station. *Energy* **2024**, *289*, 130004. [[CrossRef](#)]
23. Limbach, P.; Skoda, R. Numerical and Experimental Analysis of Cavitating Flow in a Low Specific Speed Centrifugal Pump With Different Surface Roughness. *J. Fluids Eng.* **2017**, *139*, 101201. [[CrossRef](#)]
24. Tropea, C.; Yarin, A.; Foss, J.F. *Springer Handbook of Experimental Fluid Mechanics*; Springer: Berlin, Germany, 2007.
25. Versteeg, H.K.; Malalasekera, W. *An Introduction to Computational Fluid Dynamics*; Pearson Education Limited: London, UK, 2007.
26. Ahn, S.-H.; Xiao, Y.; Wang, Z.; Luo, Y.; Fan, H. Unsteady prediction of cavitating flow around a three dimensional hydrofoil by using a modified RNG k- ϵ model. *Ocean Eng.* **2018**, *158*, 275–285. [[CrossRef](#)]
27. Singh, S.; Danish, M.; Saha, K.; Singh, B.N. Numerical simulation and analysis of fluid-structure interaction on 3D MHKF-180 and NACA4418 cavitating hydrofoils. *Ocean Eng.* **2023**, *272*, 113867. [[CrossRef](#)]
28. Ghahramani, E.; Ström, H.; Bensow, R.E. Numerical simulation and analysis of multi-scale cavitating flows. *J. Fluid Mech.* **2021**, *922*, A22. [[CrossRef](#)]
29. Menter, F.R. Two-equation eddy-viscosity turbulence models for engineering applications. *AIAA J.* **1994**, *32*, 1598–1605. [[CrossRef](#)]
30. Menter, F.R.; Kuntz, M. Adaptation of Eddy-Viscosity Turbulence Models to Unsteady Separated Flow Behind Vehicles. *Aerodyn. Heavy Veh. Truck. Buses Trains* **2004**, *19*, 339–352.
31. Qiu, N.; Zhu, H.; Xu, P.; Che, B.; Wu, J.; Zhou, W.; Wang, C. Assessment of cavitation erosion risk indicated by pressure impact exceeding material strength threshold. *Phys. Fluids* **2023**, *35*, 093307. [[CrossRef](#)]
32. Sonawat, A.; Kim, S.; Ma, S.-B.; Kim, S.-J.; Lee, J.B.; Yu, M.S.; Kim, J.-H. Investigation of unsteady pressure fluctuations and methods for its suppression for a double suction centrifugal pump. *Energy* **2022**, *252*, 124020. [[CrossRef](#)]
33. Ansys, I. *Ansys CFX Tutorials 2023 R2*; Ansys: Pittsburgh, PA, USA, 2023.
34. Karaalioglu, M.S.; Bal, S. Performance prediction of cavitating marine current turbine by BEMT based on CFD. *Ocean Eng.* **2022**, *255*, 111221. [[CrossRef](#)]
35. Lee, J.; Moshfeghi, M.; Hur, N.; Yoon, I.S. Flow analysis in a return channel of a multi-stage centrifugal pump. *J. Mech. Sci. Technol.* **2016**, *30*, 3993–4000. [[CrossRef](#)]
36. Tirunagari, S.; Hulkkonen, T.; Vuorinen, V.; Kaario, O.; Larmi, M. Proper Orthogonal Decomposition Analysis of Cross Sectional Fuel Spray Data. In Proceedings of the ICLASS, Heidelberg, Germany, 3–6 September 2012.

Disclaimer/Publisher’s Note: The statements, opinions and data contained in all publications are solely those of the individual author(s) and contributor(s) and not of MDPI and/or the editor(s). MDPI and/or the editor(s) disclaim responsibility for any injury to people or property resulting from any ideas, methods, instructions or products referred to in the content.